



# Unsteady Effects of Upstream Nozzle Wakes on Hub-Endwall Flow and Heat Transfer of an HPT Rotor

L. Chen<sup>†</sup>, Z. F. Lu and R. Dai

School of Energy and Power Engineering, University of Shanghai for Science and Technology,  
Shanghai 200093, China

<sup>†</sup>Corresponding Author Email: [chen\\_liu@usst.edu.cn](mailto:chen_liu@usst.edu.cn)

(Received April 1, 2019; accepted July 19, 2019)

## ABSTRACT

Nozzle wakes have significant effects on the heat transfer on the rotor blade and endwall surfaces. Numerical studies have been carried out in a subsonic high pressure turbine stage to investigate the rotor's secondary flow field and endwall heat transfer. Both steady and unsteady RANS analyses were accomplished for the multiple blade rows using mixing-plane and domain-scaling techniques respectively. Special attention was focused on the particular nozzle wake structure of secondary passage vortex near the hub endwall and its effects on the endwall heat transfer characteristics. Unsteady solution indicates that the passage vortex near the rotor hub is transported toward the midspan due to the blade interaction and rotation effects. In the front passage region, the time-averaged result yields higher heat transfer up to 20% than a steady one, and the transient fluctuation amplitude reaches 40% of mean values along the passage vortex moving path. In the rear passage region, the difference between steady and unsteady solutions is negligible. Current study reveals that the major difference of wake effects between an actual turbine and a linear cascade with moving bars comes from the movement of the vortical endwall passage vortex in the incoming flow.

**Keywords:** Wake; Passage vortex; Heat transfer; Endwall; Gas turbine.

## NOMENCLATURE

$C_{ax}$	axial chord	$V$	velocity (absolute one in the stator, relative one in the rotor)
$C_f$	skin friction factor	$x, y, z$	cartesian coordinates, pitchwise, radial and axial directions
$C_{pt}$	total pressure loss coefficient	$y^+$	wall friction Reynolds number
$c_p$	specific heat capacity	$\eta$	efficiency
$e$	fluid internal energy	$\rho$	density
$M$	rotor torque	$\omega$	vorticity
$Ma$	Mach number	Subscripts	
$n$	Nozzle (stator) vane	$aw$	adiabatic wall
$P$	pitch length	$w$	solid wall
$P_t$	total pressure	$l$	local value
$q$	heat flux	$N$	guide vane
$Re$	Reynolds number	$R$	rotor blade
$S$	local passage width	$r$	in relative frame
$St$	Stanton number	$s$	streamwise, or isentropic
$t$	time		
$T$	temperature or periodic time interval		
$T_u$	turbulent intensity		
$TKE$	turbulent kinetic energy		
$u_i$	velocity component		

## 1. INTRODUCTION

The modern gas turbine is developing towards high thermal efficiency and clean emissions. One of the

key measures to improve the thermal efficiency of a simple gas turbine cycle is the increase in turbine inlet temperature. As a result, the gas temperature near the endwall increases and more heat flux is

convected onto the endwall surface. Recently, local thermal damages on rotor endwalls have been reported in the first stage of a high pressure turbine. [Simon \*et al.\* \(2006\)](#) reviewed the knowledge of the convective heat transfer coefficient (HTC) distribution over turbine endwalls and emphasized to design blade cooling schemes to prevent thermal failure.

The convective heat transfer from the hot gas to cooled endwall is strongly linked to the flow field over endwall surface. HTC values depend on local flow properties, e.g. turbulence intensity. Many studies have revealed the complex rotational flow features of high turbulence intensity and vortices in annual and planar turbine cascades. Several endwall flow models of horseshoe vortices were proposed inside turbine cascades ([Langston \*et al.\*, 1980](#); [Sharma \*et al.\*, 1987](#); [Goldstein \*et al.\*, 1988](#); [Wang \*et al.\*, 1997](#)). Although there are small differences among various models, the fundamental mechanism is depicted that inlet boundary layer separates before the blade blunt leading edge into two branches of counter rotating vortices. When the pressure side horse-shoe vortex (HSV) moves through the passage under the blade to blade pressure gradient, it entrains the boundary layer fluid and evolves in a normally named passage vortex (PV) at the cascade exit which is responsible for the enhanced heat transfer regions on the central endwall surface ([Graziani \*et al.\*, 1980](#)). To minimize the effect of PV flow on the endwall heat transfer, some passive flow controlling concepts, e.g. endwall contouring, have been applied to turbine cascades ([Panchal \*et al.\*, 2017](#)). Understanding the development and transport of secondary flow plays a key role in reducing the endwall heat transfer.

The most prevailing studies of the endwall flow and heat transfer have been accomplished on stationary cascades of either stator vanes or rotor blades. One difference between a stationary experimental cascade and a real rotor lies in the unsteady effects of rotor-stator interaction. In a real machine, non-uniform exit flows from upstream stator constitute relatively time-dependant inlet flow conditions in front of the downstream rotor. [Denton \*et al.\* \(2012\)](#) emphasized the importance of unsteady loss in a turbine stage flow rather than a steady one-row cascade model. [Pullan \*et al.\* \(2006\)](#) showed that the unsteady flow loss was 10% higher than the corresponding steady one and was attributed to the unsteady inlet disturbance on the development of rotor surface boundary layer and endwall vortex structure.

Unsteady effects on the heat transfer of downstream blades including the endwall surface are predominant from the relatively moving upstream blade wakes. Moving bars are arranged before a linear cascade to simulate the wakes of nozzle guide vanes (NGV) of various passing frequencies and turbulence intensities ([Winhart \*et al.\*, 2019](#)). [Schneider \*et al.\* \(2013\)](#) showed the influence of NGV exit flow on the development of downstream rotor vortex flow. [Ciorciari \*et al.\* \(2014\)](#) studied the effects of unsteady wakes on the secondary flows in a high loaded low-pressure-turbine (LPT) cascade and

found that periodic reductions of the PV strength and the trailing edge wake and corner vortices for high passing frequencies of the bar wakes. [Park \*et al.\* \(2014\)](#) revealed that the overall heat transfer for the unsteady cases was higher and enhanced with increasing the Strouhal number due to the resulting thin boundary layer and high turbulence intensity.

Modern computational fluid dynamics (CFD) techniques provide another way to investigate the effects of unsteady wakes on the flow and heat transfer on rotor endwalls. Although some differences in heat transfer are observed due to the limitation of available turbulence models, numerical simulation provides enough ability to investigate unsteady heat transfer in a rotor passage. Computational model can be designed as close to the real machine as enough computation resources are available. [Gallus \*et al.\* \(1995\)](#) compared the results of steady and unsteady simulations and verified the higher accuracy of unsteady computation for the endwall regional flow. [El-Gabry \*et al.\* \(2010\)](#) numerically predicted small increments of unsteady HTC values on rotor endwall with specified non-uniform inlet pressure and temperature profiles. A simplified domain scaling model stator/rotor ratio of 1:1 is used since authors believed that the ratio affects a little on the prediction of the average heat transfer. Similar models of stator/rotor ratio of 1:2 are used by in [Simone \*et al.\* \(2012\)](#) and [Wang \*et al.\* \(2017\)](#) which is equivalent to reduce half the wake passing frequency. However, [Park \*et al.\* \(2014\)](#) and [Choi \*et al.\* \(2017\)](#) revealed that the time-averaged HTC on endwall surface is directly connected with the Strouhal number which is proportional to the wake bar moving frequency.

Based upon the above mentioned viewpoints, it is concluded that the understanding of incoming wake effects is obtained from simple configurations of moving bars before a linear cascade. It lacks the swirling flow features of NGV blade wake and interaction of relative moving blade rows in an actual turbine. In this paper, a 3D unsteady RANS simulation is carried out on the first stage of the E<sup>3</sup> high-pressure turbine (HPT). Rotor and stator blade numbers are scaled down to 3 and 2 passages which are much closer to the realistic HPT configuration. Special attention is focused on the interaction between the NGV wakes and the rotor endwall flows which is not observed in simulated moving bars experiments. Results predict the transient heat transfer characteristics on rotor endwall surfaces and supplement the HTC knowledge on a rotor endwall surface. It is also valuable to help turbine designer to allocate a possible region of thermal failure and to construct adequate local cooling schemes.

## 2. NUMERICAL METHODS

The following Reynolds-Averaged Navier Stokes equations without body force and external heat sources for compressible gas flow are solved for the current problem.

$$\frac{\partial \rho}{\partial t} + \frac{\partial(\rho u_i)}{\partial x_i} = 0 \quad (1)$$

$$\frac{\partial \rho u_i}{\partial t} + \frac{\partial (\rho u_i u_j + p)}{\partial x_j} = \frac{\partial}{\partial x_j} \left[ \mu_{eff} \left( \frac{\partial u_i}{\partial x_j} + \frac{\partial u_j}{\partial x_i} - \frac{2}{3} \frac{\partial u_k}{\partial x_k} \delta_{ij} \right) \right] \quad (2)$$

$$\frac{\partial \rho e}{\partial t} + \frac{\partial (\rho u_j e + p u_j)}{\partial x_j} = \frac{\partial}{\partial x_j} \left( \frac{\mu}{Pr_{eff}} \frac{\partial T}{\partial x_j} \right) + \frac{\partial}{\partial x_j} \left[ u_i \mu_{eff} \left( \frac{\partial u_i}{\partial x_j} + \frac{\partial u_j}{\partial x_i} - \frac{2}{3} \frac{\partial u_k}{\partial x_k} \delta_{ij} \right) \right] \quad (3)$$

$$\frac{\mu}{Pr_{eff}} = \frac{\mu}{Pr_{laminar}} + \frac{\mu}{Pr_{turbulent}} \quad (4)$$

$$e = c_v T + \frac{1}{2} u_i u_i \quad (5)$$

Where  $u_i$  mean Cartesian velocity components,  $\mu_{eff} = \mu + \mu_t$  for the effective viscosity includes the eddy viscosity  $\mu_t$  for the turbulence Reynolds stress closure which is from the two-equation Shear Stress Transportation model by Mentor (1994).

The numerical results presented in this paper were obtained from CFD computations using the software ANSYS CFX version 15, in which the spatial domain is discretized in element-based finite volumes. In order to achieve overall second-order accuracy in the time-dependent simulations, the second order spatial central difference scheme and the second-order backward Euler scheme for the time was selected to discretize the flow equations, turbulent kinetic energy, and specific dissipation rate.

In order to accelerate the unsteady computation, steady numerical simulations were firstly executed by using the mixing plane model, and then served the steady solutions as the initial flows for the unsteady numerical simulations. Steady convergence is accepted when the residual values of mass flow were less or equal to  $10^{-4}$  and the mass momentum and energy residual values less than  $10^{-5}$ . Dual-time step method was used in the unsteady simulations with transient sliding stator-rotor interface. Forty-eight physical time steps were selected for the time interval of three blades passing through two vane pitches. Each physical time step is iterated 20 pseudo-steps to guarantee the convergence of the unsteady numerical simulations. Time marching step was monitored by observing a local transient pressure at the rotor blade leading edge, a static temperature in rotor mid-passage as well as the mass flow rate value at the stator-rotor interface over the last five periods. The final unsteady solution is obtained from the additional 2 periods after the monitored unsteady convergence. Finally, about 32 periods were run for every computation case.

### 2.1 Solver Validation

The quality of CFD simulation, especially in the

computation of convective heat transfer, depends on two critical elements of turbulent model and mesh independence. Various turbulence models are provided in CFX software including high and low Reynolds models and shear stress transportation (SST) with  $\gamma$ - $\theta$  transition model. After reading available papers (Gallus *et al.*, 1995; El-Gabry *et al.*, 2010; Wang *et al.*, 2017) for similar turbine cascade flows with heat transfer analysis, the SST turbulence model (Menter, 1994) was used to solve the turbulent flow. The SST turbulence model combines the k- $\epsilon$  turbulence model for the outside free shear flow and k- $\omega$  turbulence model for the boundary layer inner region. It has been shown satisfied capacities of relatively low computation costs in various computations of turbine blade external heat transfer, although less accurate than large eddy simulations in some regions of local flow separation.

Mesh quality depends on the problem features and user's experiences. Since low Reynolds k- $\omega$  turbulence model is used for the inner boundary layer region, the distance from the wall of the first cell is required to maintain a value of  $y^+$  around 1.0 over all solid surfaces. Mesh aspect ratio has to be determined through the grid dependence study upon model complexity, since it depends on the user's experience and problem to solve, i.e., flow's Reynolds number.

A classic validation case for external heat transfer of turbine guide vane LS-89 (Arts *et al.*, 1992), is calculated to validate the turbulence model ability and mesh size. Four meshes have been evaluated to determine the first grid height, as listed in Table 1, which are characterized for their total mesh points, the first normal distance and non-dimensional  $y^+$ .

**Table 1 Geometric Characteristics of Four Meshes**

	GridA	GridB	GridC	GridD
Grid Points ( $\times 10^3$ )	30	50	90	120
First Grid Height (mm)	0.01	0.01	0.005	0.001
$y^+_{max}$	12	4.5	0.9	0.45
$y^+_{min}$	3	0.5	0.1	0.05

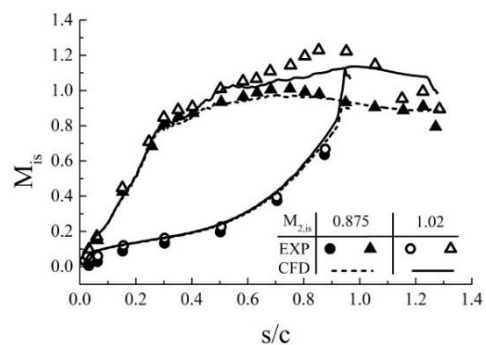


**Fig. 1. Isentropic Mach number along blade surface.**

Flow computation is validated for two exit flow

Mach numbers. Figure 1 shows the comparison of isentropic Mach number distributions along the blade surface with experimental data. The subsonic flow is well simulated whereas the transonic one is less satisfied on the suction surface where the flow Mach number is larger than 1.0. Solutions of four meshes are almost identical. The fine grid shows little advantage. It is reasoned that  $k-\omega$  model in the inner boundary layer ensures enough accuracy for  $y^+ < 10$ .

Two test cases were chosen for the assessment of heat transfer computation which is more sensitive to mesh size and turbulence closure. One is a subsonic case MUR132, and the other is a transonic case MUR235 (Arts *et al.*, 1992). Both cases cover the exit Mach number range  $0.65 < Ma < 0.927$ , which is equivalent to flow conditions in the  $E^3$  HPT case.

Figure 2 shows the HTC distributions along the blade surfaces. The main difference appears at the blade leading edge which is bluntly shaped with large curvature. Fine meshes ( $y^+ < 5$ ) can capture the boundary flow around the leading circular and predict accurate heat flux. In Fig. 2(a) of subsonic MUR132, the HTC profiles along the blade convex and concave sides match the experimental data. Fig. 2(b) of transonic MUR235 calculation results match experimental data only in the first 20 percent part and have an evident discrepancy in the aft part, which is attributed to the inability of the turbulence model to predict flow transition with high inlet turbulence intensity.

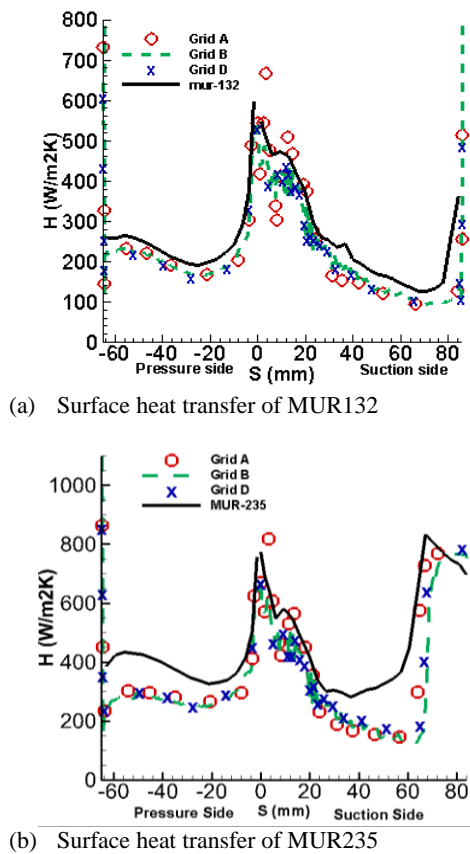


Fig. 2. RANS predictions of HTC of case MUR132 and MUR235.

From the validation, we conclude that the convective heat transfer on the blade surface predicted with the SST turbulence model is acceptable accurate on a mesh with its first grid height of  $y^+ < 5$ . Actual first grid height is determined after the steady computation is finished and mesh is refined until the criteria  $y^+ < 5$  is satisfied. It is obligated in later flow analysis as in similar studies on turbine endwall heat transfer (El-Gabry *et al.*, 2010; Wang *et al.*, 2017).

## 2.2 Geometry and Boundary Conditions

The baseline geometry of the present study case comes from the first HPT stage of  $E^3$  engine (Timko, 1984), which has 46 stator guide vanes and 76 rotor blades. In the unsteady computation, the domain scaling approach is used to simulate the relative movement of stator and rotor to save the computational resources. To capture the unsteady features of rotor endwall heat transfer, a model of stator/rotor ratio 2:3 is the minimum element closest to actual configuration, in which the effect of blade loading change is negligible (Rai, 1987). Therefore, the rotor blade number is reduced to 69 and chord length is enlarged by 76/69. The stator vane geometry is maintained to duplicate the original stator exit flow structure.

The simulation boundary conditions are specified as provided in the  $E^3$  turbine performance test report. The domain inlet is located at 50% axial chord upstream of the NGV leading edge with specified total pressure and temperature of 344.7 Pa, and 709 K, respectively. Uniform turbulence intensity of 10% and the integral length scale of 7.5 mm are also given at the turbine inlet. The radial variation of inlet flow conditions is not considered for simplicity, since both experimental (Simone *et al.*, 2012) and computational results (Wang *et al.*, 2017) show negligible influences on the rotor surfaces.

The exit of the domain is extended two axial chords downstream of the rotor blade trailing edge. A static constant pressure of 150 kPa as measured in the experiment is applied at the midspan and a radial equilibrium is enforced. No slip boundary conditions are applied to all solid walls in the domain, including airfoil, hub and casing. The rotor rotating speed was 8,283 rpm. The working fluid of the turbine was ideal air gas. The boundary conditions for unsteady computation are the same as steady computations, except the sliding stator-rotor connecting interface instead of mixing plane.

Each vane and blade passages are meshed with a commercial software NUMECA AutoGrid5. Grid topology is the 4H-O meshing in which an O-block wraps the airfoil and forms fine meshes over the solid surface. Four H-blocks surrounded the O-block to improve the quality of the mesh. Final mesh is shown in Fig. 3. As in the previously mentioned solver validation cases, the height of first grid node from the solid wall is set 0.001 mm and the normalized wall distance  $y^+$  on solid walls was less than 2 to meet the requirement of SST turbulence model with  $\gamma-\theta$  transition model. However, the total number of grid points in each blade row is gradually increased for the mesh independent solution. Variations of steady nozzle efficiency ( $\eta_N$ ) and steady rotor torque ( $M$ ) are

**Table 2 Grid independence**

	2Nozzle	Blade	2Nozzle&3Blade		
Grid Level	Grid points.( $\times 10^3$ )	Grid points.( $\times 10^3$ )	Grid points.( $\times 10^6$ )	$\eta_N$	$M(N\cdot m)$
Coarse	363	253	1.49363	0.9571	26.3169
Medium	625	527	2.30625	0.9577	26.3658
Fine	1163	968	5.231163	0.9586	26.3835
Excellent	1711	1505	7.941711	0.9588	26.3805

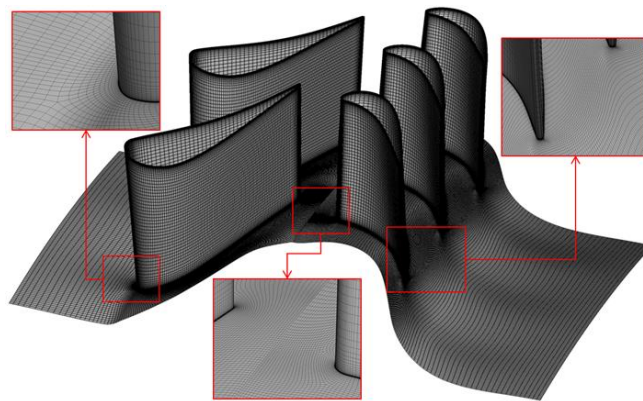


**Fig. 3. Computational mesh.**

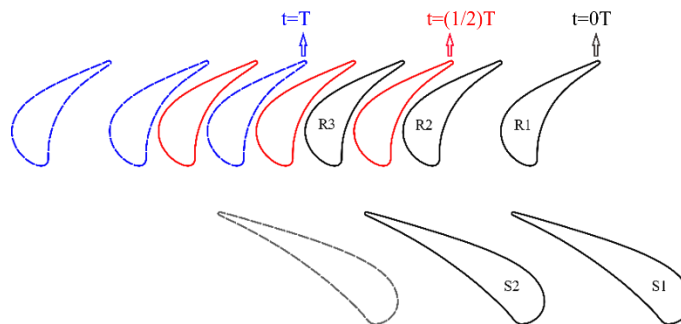


**Fig. 4. Periodic rotor positions relative to nozzle vanes.**

compared among four meshes of different density levels as listed in Table 2. As the grid number reaches the fine level, variations of nozzle efficiency and blade torque are neglectable. Therefore, all results presented hereafter are obtained from a fine mesh of total grid points of 5.23 million.

### 3. RESULTS AND DISCUSSION

Simulation of the unsteady flow in the E<sup>3</sup> HPT rotor passage achieves acceptable convergence after 8 computational physical steps. Final results of the last period are presented in this paper to demonstrate the transient flow and heat transfer characteristics. Figure 4 shows the rotor positions relative to guide vanes. One computation physical step T covers two NGV pitch intervals. Since 2 vanes are coupled by 3 blades, each blade undergoes two sub-periodic cycles within one calculated physical time step. When one rotor blade (R1) moves from stator vane 1 (S1) to vane 2 (S2), the instantaneous flow fields

between R1 and R2 are visualized for analysis of unsteady wake effects.

#### 3.1 Nozzle Exit Flow

The isentropic Mach number profiles on the NGV surface at the hub 5% span are extracted from the steady computations and compared with available experiment datasets in Fig. 5. Except some small discrepancies may be observed at the mid-chord of the pressure surface (PS) and 80% chord of suction surface, the overall quality of numerical results are satisfying. The flow velocity is highest in the NGV hub region because of the free vortex design. Therefore, the maximum isentropic Mach number value inside the NGV is lower than sonic flow condition. Mesh size and turbulence closure which have been validated for the subsonic case in Fig. 3 ensure credible NGV exit flow simulation to provide realistic NGV wake characteristics and hub endwall vortical structures.

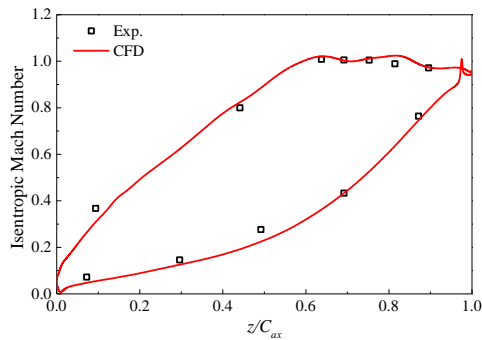


**Fig. 5. Isentropic Mach number on the blade at 5% span.**

Figure 6 shows the NGV time-averaged flow variables on the cross-passage plan downstream at axial position  $z/C_{ax,N}=1.1$ . In Fig. 6(a) the colored flood plot of total pressure loss coefficient  $C_{pt}$  shows the NGV wake along the span close to the nozzle trailing edge. In addition to the midspan wake of blade surface boundary layer, a loss core near the hub endwall is also visible at the hub and suction side corner which is regarded as the PV core. Fig. 6(b) shows the radial variation of static pressure from the tip to the hub. Then inside the nozzle wake, the low momentum fluids move downward from the tip to hub because of the imbalance of centrifugal force and the radial pressure gradient. Both effects of the PV movement and the wake's radial movement produce an extended zone of loss close to the nozzle hub endwall. Figures 6(c) and 6(d) show the enlarged views of the SS-hub corner in Fig. 6(a) for both steady and unsteady calculations. Over the  $C_{pt}$  contour plots are overlaid the streamwise vorticity (helicity) isolines in dashed lines. The vortex center is lifted off the endwall surface and does not coincide with the loss centroid, which indicates that the radial movements of blade wake fluids bring extra losses accumulated at the endwall. Compared with those wakes produced by moving bars, special NGV wake structure is formed to have stronger vortical turbulence effects. It reflects the significance to investigate the wake effect of upstream blade row on the hub endwall of downstream blade row.

Figure 7 shows the time-averaged turbulence intensity ( $T_u$ ) at the nozzle exit plane. The wake and secondary vortices generate high turbulence intensity regions. In Fig. 7(a), there is a high turbulence intensity region on the vane's suction side and hub endwall, which is caused by the PV vortical flow in the corner region. The area of high turbulence intensity in Fig. 7(a) is well matched with the area of high total pressure losses in Fig. 6(a), which has also been verified in the LDV measurements in Matsumura (2008) experiment. Figure 7(b) shows the pitchwise distributions of turbulence intensity at 1% and 50% span heights. It is evident that the turbulence intensity near the hub endwall is stronger than at midspan due to the additional endwall passage vortex and radial wake movement. Another important feature in Fig. 7(b) is that the wake of endwall PV extends over about 70% of NGV pitch starting from  $x/S=0.20$ , whereas at midspan the wake

occupies only about 20% pitch as a spike. It has not been indicated in simulated cascade experiments (Ciorciari *et al.*, 2014; Park *et al.*, 2014) by moving bars, in which wake has a uniform structure along the cascade height. It can be anticipated that increased turbulence intensity affects differently on the endwall flow as it ever does on blade surfaces (Olson *et al.*, 2011). It is anticipated to distinguish the effects of nozzle secondary vortices on hub-endwall flow and heat transfer of its downstream rotor.

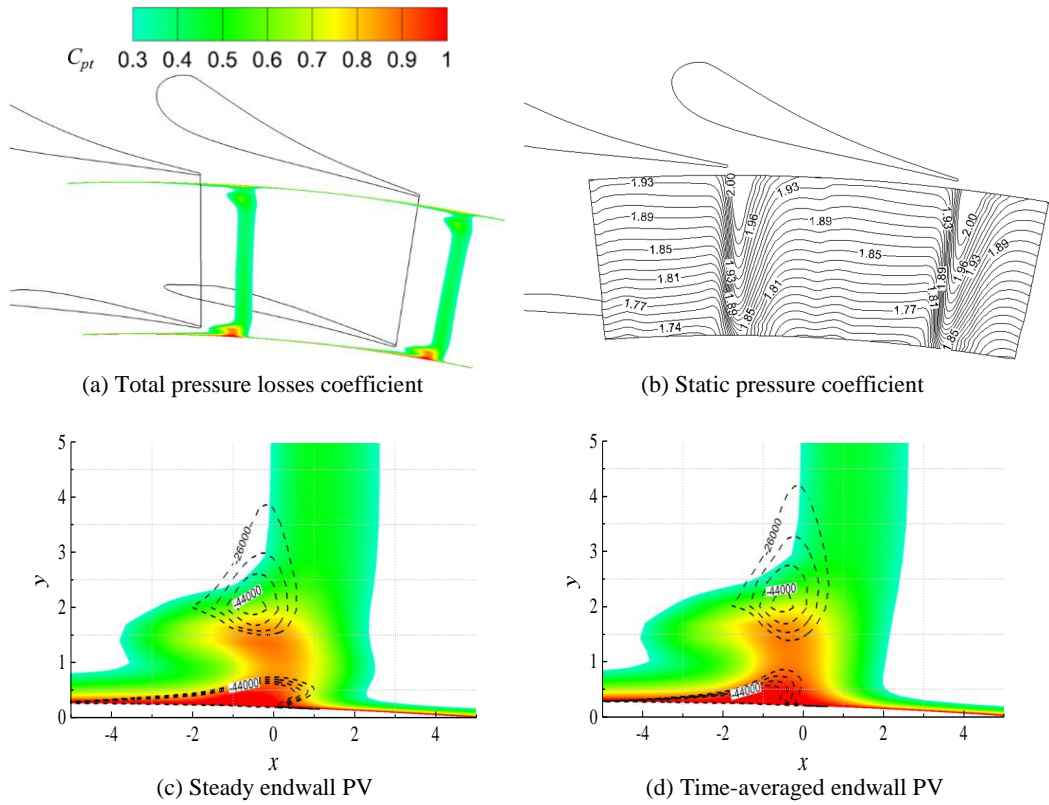
Figure 7(c) shows the pitch-averaged turbulence intensity along the NGV span. Both results of steady and unsteady cases are plotted, which are hard to distinguish their differences. It has to be noted that although the nozzle flow is slightly disturbed by the relative movement of the downstream rotor, it is potential interaction which has limited effects on the upstream flow field. Steady flow solution is nearly the same as the time-averaged unsteady one except the passage vortex is lifted a small distance further from the hub wall as shown in Fig. 6(d).

### 3.2 Rotor Inside Flow

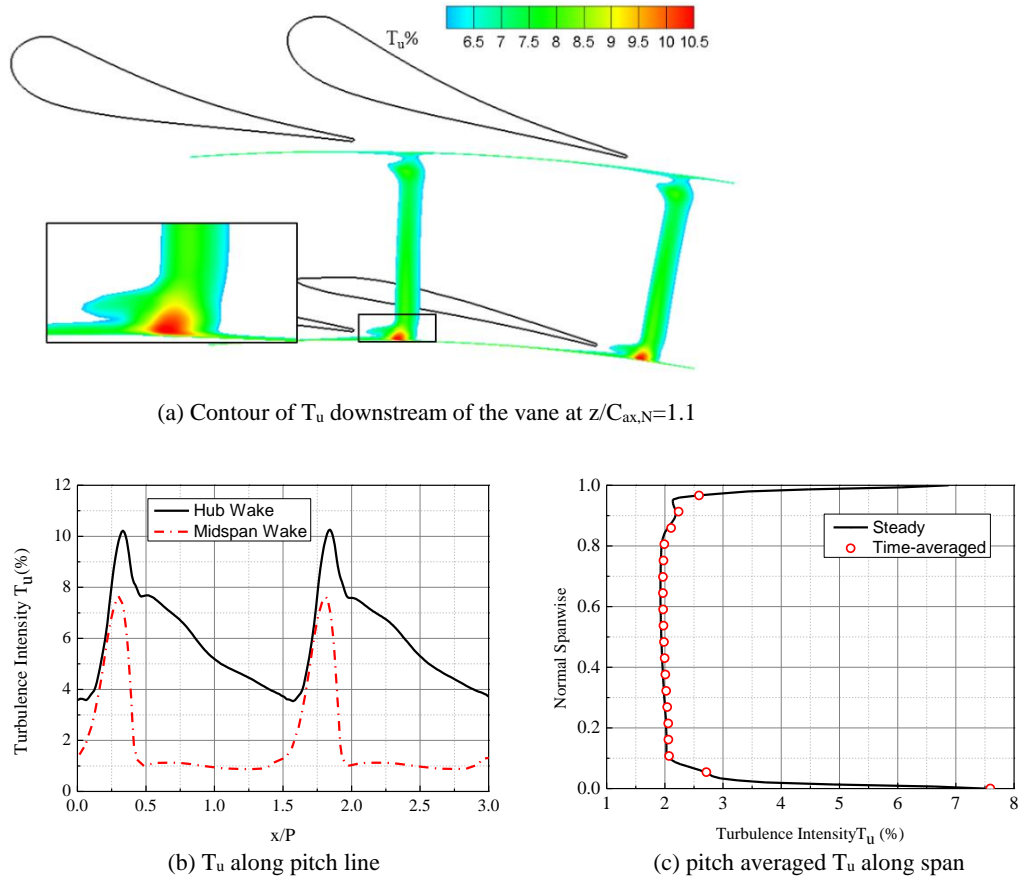
Incoming NGV wakes have two effects on the flow in the downstream rotor passage. One is the increased turbulence intensity ( $T_u$ ) and the other is the reduced flow velocity to increase rotor positive incidences. Since the wake characteristics vary along the nozzle span as shown in Fig. 7(b), the possible effects of incoming wakes are then anticipated to be different between the midspan and endwall.

Figure 8(a) shows an instantaneous contour of turbulence intensity at the rotor midspan. Incoming wakes sweep over rotor blade surfaces and get propagated inside the blade row. The dashed lines in the figure show the wake's moving paths of nozzle S1, which is distorted at the blade leading edge due to the blade interaction. When the nozzle's wake enters the rotor row, it is stretched by the blade to blade velocity gradient and pushed toward the adjacent suction side.

Figure 8(b) shows the time-resolved turbulence intensity contours at the 1% span close to the hub endwall, on which two dashed lines are drawn. The long dashed line depicts the moving path of the rotor's endwall PV, while the short dotted line depicts the path of nozzle wakes. In addition, a rotating arrow indicates the nozzle's endwall PV. The values and areas of high  $T_u$  become larger and more complicated than at the midspan. In addition to the wakes being smashed and stretched by the moving blade, two PVs appear on the rotor endwall and generate the highest turbulent streak at the leading edge and cross to the SS of the neighboring blade. Instantaneous  $T_u$  contours vary for the two adjacent rotor passages since 2 nozzle wakes are periodically phased among 3 blade passages. As a result, it is derived that the simulated wakes of moving bars can only model the nozzle midspan wakes with periodic turbulence intensity, rather than the vortical endwall PV from nozzle cascade flow. Periodic fluctuations should appear on the endwall for heat transfer because of the periodic sweeping vortical inlet flow.



**Fig. 6. Flow variable distributions behind NGV at  $z/C_{ax,N}=1.1$ .**



**Fig. 7. Turbulence intensity  $T_u$  in NGV wake flow.**

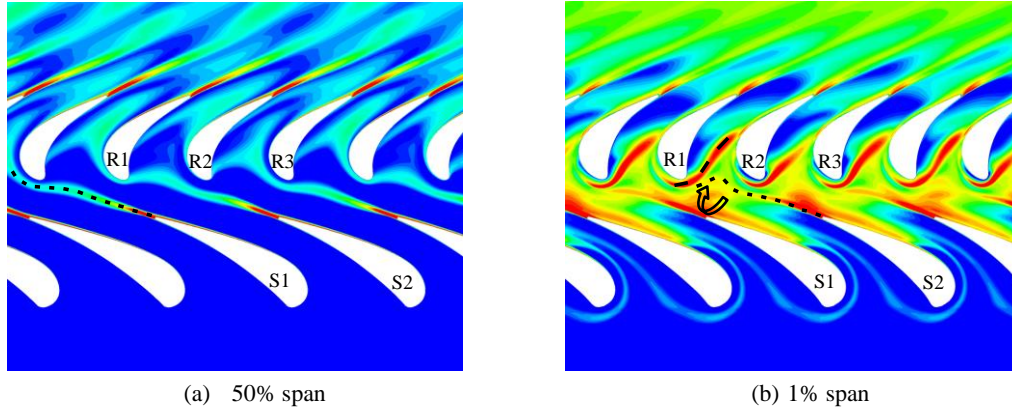


**Fig. 8. Contours of turbulence intensity  $T_u$ .**

Figure 9 shows the contour plots of TKE and helicity isolines on three cross channel sections (at  $z/C_{ax,R}=0.5, 0.8, 1.1$ ) from steady and unsteady solutions. The time-averaged unsteady solution has higher values than the steady one on each cross-section surface inside the passage, because the nozzle PV core remains at the blade corner and interacts with rotor PV intensifying the turbulent mixing. But on the exit plan  $z/C_{ax,R}=1.1$ , the difference is negligible. This indicates that incoming wake mainly affects on the front part of rotor endwall.

At the time instant of  $(0/6)T$ , compared to the others, the passage vortex approaches suction surface closer at  $z/C_{ax,R}=0.5$ . It is produced by the incoming nozzle passage vortex. As the blade moving along the pitch line, the nozzle PV flows downstream in the rotor passage. For this reason, the PV center at  $z/C_{ax,R}=0.8$  is displaced far from endwall at  $(1/6)T$  compared to the previous time point. At the plane downstream of the rotor at  $z/C_{ax,R}=1.1$ , regions of passage vortex and wake are observed. It is obvious that the scope of passage vortex expand when the time arrives at  $(2/6)T$ . In addition, TKE values in the wake region vary during this time interval.

### 3.3 Endwall Friction Coefficient

Convective heat transfer on a solid wall surface is strongly linked with the state of the boundary layer over the wall. In addition to the near-wall limit streamlines, skin friction coefficient (SFC)  $C_f$  is usually used to reflect the near-wall boundary layer flow. SFC value is a unique physical index to reflect the flow's laminar, transition, turbulent and separated states. On a flat wall, Stanton number is related with  $C_f$  and Nusselt number through the Reynolds analogy.

$$St = \frac{Nu}{Re \cdot Pr} = \frac{1}{2} \frac{C_f}{Pr} \quad (6)$$

The Prandtl number  $Pr$  is a fluid property varying little in the flow and is regarded as a constant value. Stanton number is then proportional to the SFC value which is then used as an alternative measure to investigate the convective heat transfer on a blade endwall surface.

Figure 10 shows the SFC distributions on the hub for steady and unsteady conditions. There are three regions of attention: saddle point region (Region I), corner region upstream of the suction surface (Region II) and downstream of lift-off line (Region III). Figures 10(a) and (b) show the time-averaged wall friction coefficients for the unsteady case are lower than for the steady case in Region I and Region II. It implies that the vortex influences on the hub get weaker in an unsteady case.

Figure 11 shows three instantaneous SFC contours on the hub endwall. As the blade moves, the NGV hub wake with PV core affects the flow structure around saddle point. The shape of Region I deforms periodically. It travels downstream into the rotor passage, and its effects on Region II go fading. The SFC values in this region increase gradually. For the same reason, the SFC values in Region III decrease at first and then increase.

### 3.4 Endwall Heat Transfer

Since the metal temperature under high inlet gas temperature is the first challenge of HP turbine design, the HTC distribution on endwall surface is more important than flow efficiency at the component designing stage. The non-dimensional parameter, Stanton number ( $St$ ), is used in this paper to demonstrate the non-uniform and transient endwall heat transfer characteristics. Stanton number is defined as

$$St = \frac{q_w / (T_{aw} - T_w)}{\rho c_p V_N} \quad (7)$$

where  $q_w$  is heat flux,  $T_{aw}$  is adiabatic wall temperature,  $T_w$  is wall temperature, and  $V_N$  is velocity at nozzle exit. In a steady simulation, two separate computations are usually carried out with the adiabatic wall for  $T_{aw}$  and the isothermal wall for  $q_w$  respectively. However, it is too much expensive to do it in an unsteady simulation. The approximate solution of the thermal boundary layer on a flat plate by White (1974) is used to avoid the overload of calculating  $T_{aw}$ . Adiabatic temperature  $T_{aw}$  is calculated by the local isentropic velocity  $V_{s,i}$  and the static fluid temperature  $T$  via a recovery factor  $r$ :

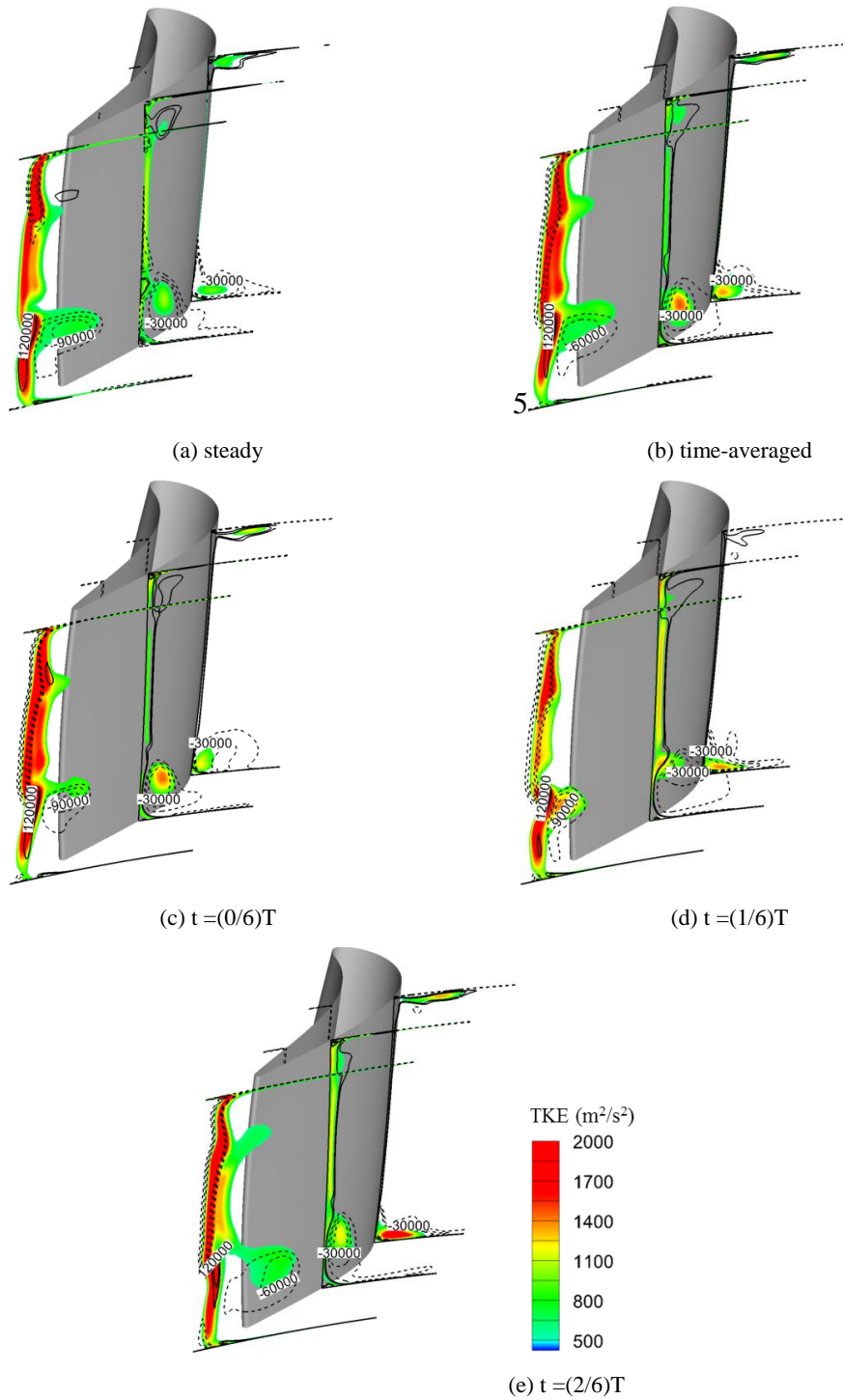
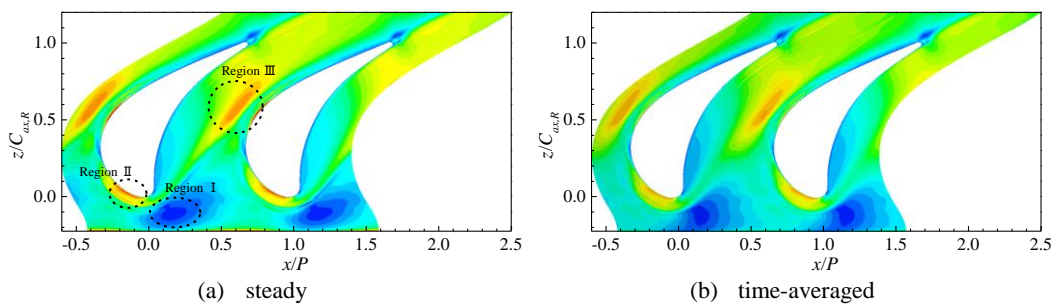


**Fig. 9.** Turbulent kinetic energy and stream-wise vorticity at three axial planes.



$$T_{aw} = T + r \cdot \left( \frac{V_{s,l}^2}{2} \right) \quad (8)$$

where  $r = \sqrt{Pr}$  is the fluid Prandtl number which can be regarded as a constant for an ideal gas. The  $V_{s,l}$  value is calculated by the ratio of local static pressure and inlet total pressure. In this way,  $T_{aw}$  can be approximated simultaneously in the time-resolved solution of the unsteady endwall heat transfer.

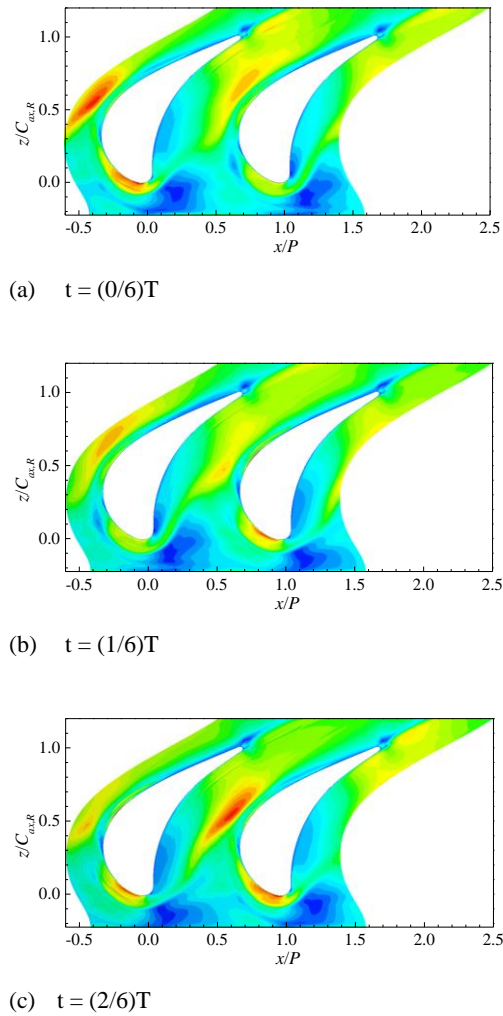


**Fig. 11. Instantaneous skin friction coefficient contours.**

Figures 12(a) and (b) show respectively the steady and time-averaged Stanton number distributions on the hub endwall. There are four distinct regions influenced considerably by stator passage vortex on the hub: upstream passage vortex region (UPVR), leading edge region (LER), lift-off line region (LLR) and trailing edge pressure surface region (TER), which are shown in Fig. 12(b). Since rotor-stator interface is treated as pitch averaged by mixing plane approach for the steady case, there is no NGV passage vortex entering the rotor passage, and the values of Stanton number in UPVR are lower than time-averaged results. In the LER and LLR regions, the maximum Stanton number in the steady

condition is higher than the time-averaged result, because of the higher wall friction in the steady case as shown in Fig. 10. Figure 12(c) shows the amplitudes of HTC fluctuation in the percentage of its time-averaged value within one time period. High fluctuation appears before the blade leading edge where the NGV secondary flow maintains its vortical structure on its path line. When it enters the rotor passage, it is distorted and dispersed on the pressure side and gets mixed with rotor's HSV pressure side leg. The turbulence intensity along the PV moving path is augmented as the blade moves over NGV trailing edges.

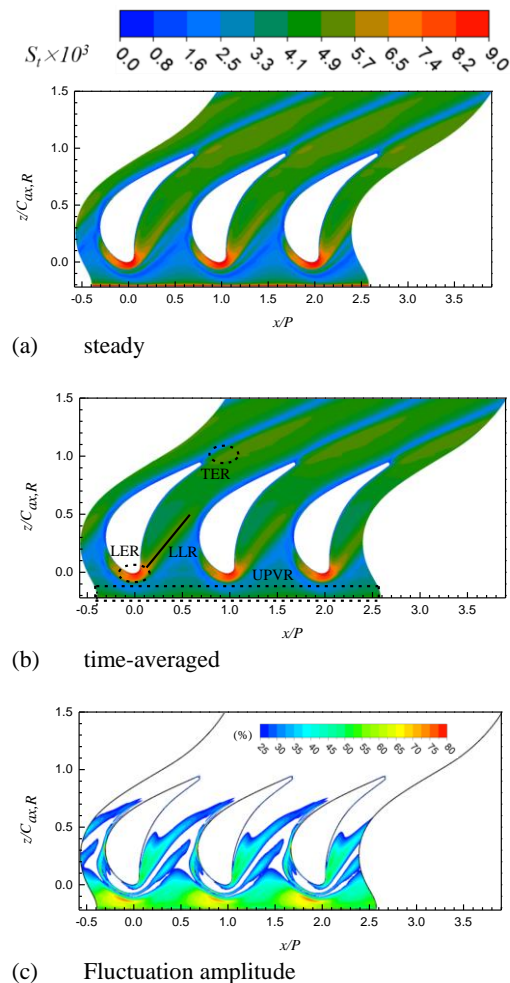


**Fig. 12. Endwall distributions of Stanton number.**

Figure 13 shows the pitchwise distributions of Stanton number on the rotor endwall at four axial positions in an attempt to quantify the influence of incoming wakes. The abscissa direction is from the pressure side to suction side on the hub BTB surface and coordinates of the abscissa are the relative distances of the local channel BTB width. The time-averaged profile is also depicted with its fluctuation amplitudes in the form of an error bar.

Figure 13(a) shows the Stanton distribution at  $z/C_{ax,R} = -0.05$  before the leading edge. Time-averaged value is higher than the steady one over the

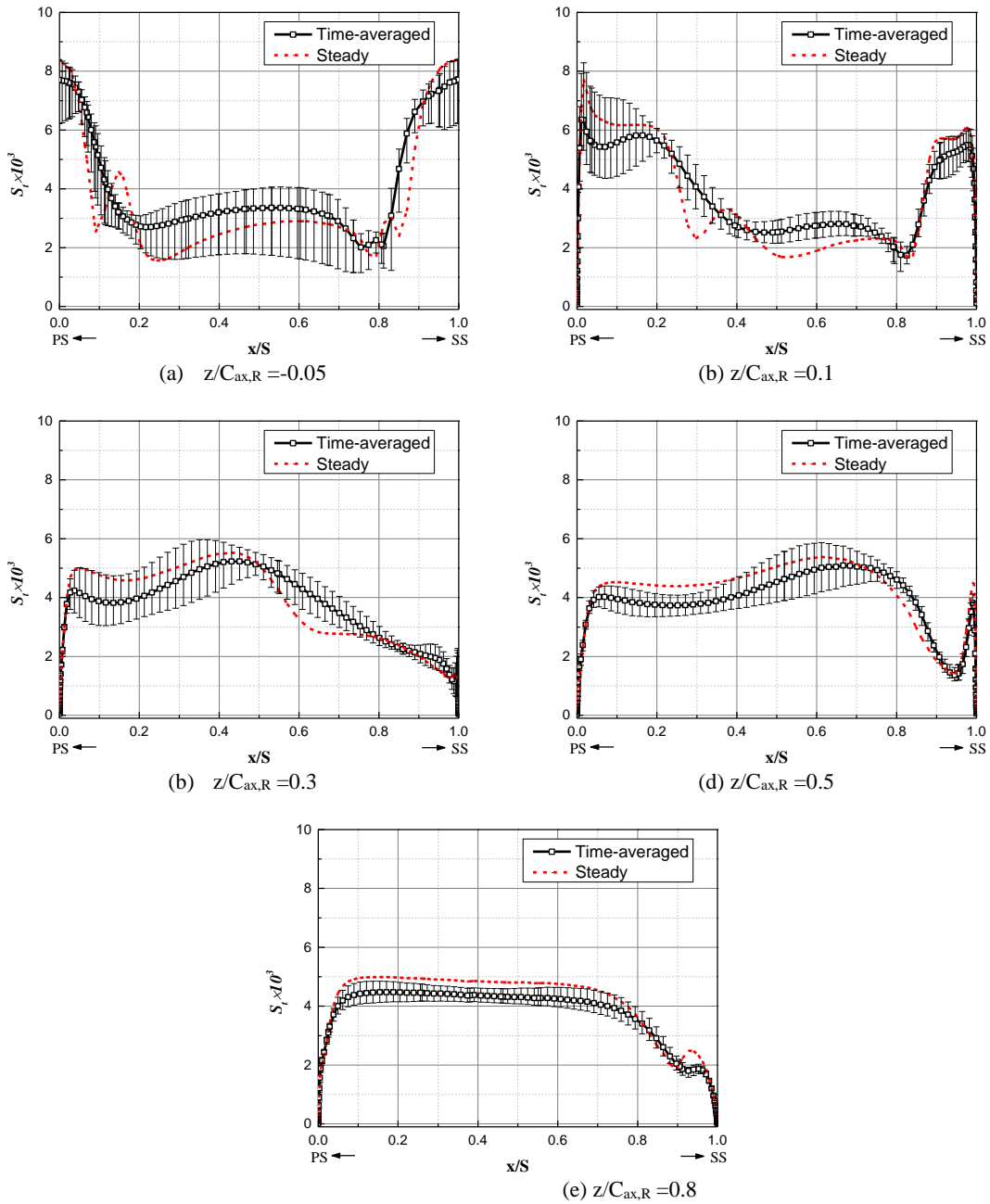


**Fig. 13. Pitchwise profiles of Stanton number at different axial positions.**

pitch line. Another important feature in Fig. 15(a) is that the first large fluctuations appear in the center of blade passage and their amplitudes achieve nearly 50% of the steady case. The second fluctuation regions are close to the blade leading edge. Obviously, the increases in Stanton number come from the near wall effects of NGV wake sweeping. The difference between the steady and unsteady solutions is much less than the fluctuation values, which is of concern to evaluate material thermal default.

Figure 13(b) shows the local heat transfer profile at  $z/C_{ax,R}=0.1$  close to blade leading edge inside blade passage. As described in Fig. 12(a), the heat transfer is high in front of the leading edge because of the

impingement and separation of inlet boundary layer fluids. The heat transfer for the steady case is similar or slightly lower than the time-averaged case. In particular, for the middle region, both cases are nearly the same. However, instantaneous heat transfer near PS and SS walls fluctuate obviously around the time-averaged values. Its amplitude is higher on PS than on SS. It is attributed to the effect of nozzle endwall PV which impinges on the rotor PS surface and generates high turbulence intensity in addition to the relative inlet flow boundary layer approaching blade leading edge.

Figure 13(c) shows the local heat transfer distribution at  $z/C_{ax,R}=0.3$ . The peak HTC is moved into the central passage about  $x/S=0.4$ , which is the

result of PV movement. The region of heat transfer fluctuation is extended between the PV center and pressure side ( $0.1 < x/S < 0.5$ ) due to the strong effects of PV sweeping. Another important feature is that the smoothing effect of the unsteady wake. In the middle passage ( $x/S=0.8$ ) of the steady case, there is an abrupt HTC rise due to the HSV suction leg. But the step is smoothed in the unsteady case, because the PV changes its position as the incoming wake appears or not. In that region, HTC values are also higher than in the steady case.

The HTC local distribution at  $z/C_{ax,R}=0.5$  is shown in Fig. 13(d). The passage vortex has moved close to the suction side of the neighboring blade which is visible in Fig. 10. The high HTC region is corresponding and located at  $0.4 < x/S < 0.8$ . Heat transfer of steady case is similar to time-averaged result except for the fluctuations in the PV region. Close suction side  $0.8 < x/S < 1.0$ , HTC drops quickly until very close to the suction surface, HTC rises abruptly. It is reasoned that HSV suction leg has dissipated and a new corner vortex appears in the endwall and suction side corner. As on Fig. 12(a), it is observed that a new  $C_f$  zone appears after blade mid-chord (depicted in blue color).

Figure 13(e) depicts the HTC profile at  $x/C_{ax,R}=0.8$ , which is close to the passage throat where the fluid accelerates to the highest flow velocity. Small fluctuations appear because the incoming wake has been dissipated in the accelerating flow. The influence of wake is reduced. Compared with Fig. 12, the heat transfer in the aft passage intends to be uniform and increases overall HTC due to the high flow velocity and turbulence intensity.

One special feature of Fig. 13(e) is the reduction of endwall HTC near the suction side. It is contradictory to the knowledge obtained in experiments of linear cascade with moving bars (Park *et al.*, 2014; Choi *et al.*, 2017) where endwall heat transfer demonstrates high HTC in the SS and hub endwall corner because of the influence of passage vortex. Since there are no direct corresponding experiment data available to validate our simulation, we referred a similar computation case of the E<sup>3</sup> HP turbine stage by El-Gabry (2010), who validated their computation method through indirect comparison with other available test data. A small area of low heat transfer appears at the SS and hub corner. In this paper, authors reasoned that the difference from cascade experiments comes from the rotation effect, which drives the PV moving radially towards the casing. In Fig. 12, it is shown that the PV is lift off the endwall and new boundary layer is reattached to the endwall surface.

The present results indicate that the incoming NGV secondary vortices increase the rotor endwall heat transfer significantly. In particular, the effect is strong at the inlet and the front half of the endwall surface. But on the rear endwall surface, heat transfer coefficient levels are equivalent in both steady and unsteady cases. In addition to the large spatial variations of heat transfer distribution as in a stator (steady case), local temperature fluctuations occur along the moving path of passage vortex in a rotor

passage with incoming NGV wakes. Therefore, large temperature gradients together with large local transient temperature variations lead to possible failure. Therefore, a cooling system is designed to be different in various regions to consider not only the spatial temperature gradients but also the fluctuation amplitudes. Especially, strong passage vortex and incoming secondary NGV vortices block the jet coolant from the leading and suction-side film cooling holes. Thus, special film cooling flows is necessary for the fluctuating cross flow conditions.

#### 4. CONCLUSIONS

Detailed computational studies have been performed specifically to investigate the effects of nozzle secondary vortices on the endwall flow and heat transfer of downstream rotor in a single HPT stage. The exit flow structure of nozzle guide vane, the endwall skin friction coefficient and heat transfer of rotor hub endwall have been computed using an URANS calculation. Time-averaged solutions have been compared with corresponding steady computation ones to evaluate the effect of unsteadiness due to the wake passage.

The NGV wakes have evident passage vortex characteristics and strong turbulence intensity near the endwall, which is less influenced by the rotor's movement. The maximum value of the turbulence intensity at the nozzle passage vortex region is as much as 20%. The nozzle passage vortex maintains its vortical shape and moves with the developing rotor passage vortex like a negative jet wake because it has relatively low velocity.

In the front half rotor endwall surface, the nozzle passage vortex and the rotor's pressure side horseshoe vortex mix with each other and enhance the near-wall turbulence intensity. The heat transfer is raised along their moving paths. The nozzle passage vortex induces large perturbations of the rotor flow field. The periodic fluctuations of the local turbulence intensity and heat transfer coefficient reach 30% and 10% respectively.

In the rear half endwall, the nozzle wakes are diminished in the accelerating flow. The rotor passage vortex core is accumulated on the rotor suction surface and lifted off the end wall up to  $Y/H=0.40$  near the midspan because of the centrifugal force. Endwall heat transfer distribution gets to be uniform except in the suction and pressure side corners where new corner vortices occur like in a steady case.

The predicted effects of the unsteady nozzle wakes on the heat transfer coefficients on the rotor endwall surface are found to be less than those obtained in low speed linear cascade experiments. It is attributed to the real engine conditions of high Reynolds and Mach numbers as well as the rotating frame in the simulations. The overall time-averaged heat transfer coefficients predicted in the unsteady computation have nearly the same values as in the steady computation. But significant fluctuations of thermal load occur in the front half of cascade endwall which preserves attention to prevent local thermal failure.

#### ACKNOWLEDGEMENTS

The authors acknowledge the financial funding from National Science Foundation of China under the Research Project (No. 51276116). Master graduate student Mr. Yu Ban has also contributed in building the first computation model.

#### REFERENCES

- Arts, T. and M. Lambert de Rouvroit (1992). Aero-thermal performance of a two-dimensional highly loaded transonic turbine nozzle guide vane: a test case for inviscid and viscous flow computations. *Journal of Turbomachinery-transactions of the ASME* 114(1), 147-154.
- Choi, S. M., J. S. Park, H. Chung, S. Park and H. H. Cho (2017). Upstream wake effect on flow and heat transfer characteristics at an endwall of first-stage blade of a gas turbine. *Experimental Thermal and Fluid Science* 86, 23-36.
- Ciorciari, R., I. Kirik and R. Niehuis (2014). Effects of unsteady wakes on the secondary flows in the linear T106 turbine cascade. *Journal of Turbomachinery-transactions of the ASME* 136(9), 091010.
- Denton, J. and G. Pullan (2012). A numerical investigation into the sources of endwall loss in axial flow turbines. *ASME Turbo Expo 2012: Turbine Technical Conference & Exposition, Copenhagen, Denmark*.
- El-Gabry, L. A. and A. A. Ameri (2010). Comparison of steady and unsteady RANS heat transfer simulations of hub and endwall of a turbine blade passage. *Journal of Turbomachinery* 133(3), 031010.
- Gallus, H. E., J. Zeschky and C. Hah (1995). Endwall and unsteady flow phenomena in an axial turbine stage. *Journal of Turbomachinery-transactions of the ASME* 117(4), 562-570.
- Goldstein, R. J. and R. A. Spores (1988). Turbulent transport on the endwall in the region between adjacent turbine blades. *Journal of Heat Transfer-transactions of the ASME* 110(4a), 862-869.
- Graziani, R. A., M. F. Blair, J. R. Taylor and R. E. Mayle (1980). An experimental study of endwall and airfoil surface heat transfer in a large scale turbine blade cascade. *Journal of Engineering for Power-transactions of the ASME* 102(2), 257-267.
- Langston, L. S. (1980). Crossflows in a turbine cascade passage. *Journal of Engineering for Power-transactions of the ASME* 102(4), 866-874.
- Matsunuma, T. (2008). Effects of nozzle secondary vortices on unsteady hub-endwall flow of a turbine rotor. *Journal of Power & Energy Systems* 2(3), 331-337.
- Menter, F. R. (1994). Two-equation eddy-viscosity turbulence models for engineering applications. *AIAA Journal* 32(8), 1598-1605.
- Olson, S. J., S. Sanitjai, K. Ghosh and R. J. Goldstein (2011). Effect of wake-disturbed flow on heat (mass) transfer to a turbine blade. *Journal of Turbomachinery-transactions of the ASME* 133(1), 011015.
- Panchai, K. V., S. Abraham, A. Roy, S. V. Ekkad, W. Ng, A. S. Lohaus and M. E. Crawford (2017). Effect of endwall contouring on a transonic turbine blade passage: heat transfer performance. *Journal of Turbomachinery* 139(1), 011009.
- Park, J. S., E. Y. Jung, D. H. Lee, K.M. Kim, B.S. Kim, B.M. Chang and H. H. Cho (2014). Effects of unsteady wake on heat transfer of endwall surface in linear cascade. *Journal of Heat Transfer-transactions of the ASME* 136(6), 061701.
- Pullan, G. (2006). Secondary flows and loss caused by blade row interaction in a turbine stage. *Journal of Turbomachinery-transactions of the ASME* 128(3), 484-491.
- Rai, M. M. (1987). Navier-Stokes simulations of rotor/stator interaction using patched and overlaid grids. *Journal of Propulsion and Power* 3(5), 387-396.
- Schneider, C. M., D. Schrack, M. Kuerner, M. G. Rose, S. Staudacher, Y. Guendogdu and U. Freygang (2013). On the unsteady formation of secondary flow inside a rotating turbine blade passage. *Journal of Turbomachinery-transactions of the ASME* 136(6), 061004-061004-10.
- Sharma, O. P. and T. L. Butler (1987). Predictions of endwall losses and secondary flows in axial flow turbine cascades. *Journal of Turbomachinery-transactions of the ASME* 109(2), 229-236.
- Simon, T. W. and J. D. Piggush (2006). Turbine endwall aerodynamics and heat transfer. *Journal of Propulsion & Power* 22(2), 301-312.

- Simone, S., F. Montomoli, F. Martelli, K. S. Chana, I. Qureshi and T. Poverly (2012). Analysis on the effect of a nonuniform inlet profile on heat transfer and fluid flow in turbine stages. *Journal of Turbomachinery-transactions of the ASME* 134(1), 011012.
- Timko, L. P. (1984). *Energy Efficient Engine high pressure turbine component test performance report*. United States.
- Wang, H. P., S. J. Olson, R. J. Goldstein and E. R. G. Eckert (1997). Flow visualization in a linear turbine cascade of high performance turbine blades. *Journal of Turbomachinery-transactions of the ASME* 119(1), 1-8.
- Wang, Z., D. Wang, Z. Liu and Z. Feng (2017). Numerical analysis on effects of inlet pressure and temperature non-uniformities on aerothermal performance of a HP turbine. *International Journal of Heat and Mass Transfer* 104, 83-97.
- White, F. M. (1974). *Viscous Fluid Flow*. McGill-Hill, Inc.
- Winhart, B., M. Sinkwitz, A. Schramm, D. Engelmann, F. D. Mare and R. Mailach (2019). Experimental and numerical investigation of secondary flow structures in an annular LPT cascade under periodically wake impact – Part 2: numerical results. *Journal of Turbomachinery* 141(2), 021009.